Development of a Two-Dimensional Mathematical Model for Stress and Velocity Distribution in a Packed Bed

S. SARKAR and G.S. GUPTA

Cavity or raceway in gas cross-flow condition is common in various industrial processes such as blast furnace, COREX process, granular drying, *etc*. Raceway size and shape play an important role in the aerodynamics of these processes. There are many studies to determine the raceway size; however, minimal work is available on determination of its shape. Knowledge of stress distribution is a necessary precursor to determine the shape of the raceway. Therefore, an attempt has been made to predict the stress condition at the raceway boundary under gas cross-flow condition based on continuum model. Two-dimensional (2-D) k-ε turbulence model has been solved for the gas flow, whereas solid phase has been represented by 2-D static stress equations. Computed results have been validated with experiments. Based on numerical results, normal stress distribution along the slip planes or characteristics has been plotted and it has been found that raceway boundary is an *isostress* boundary.

DOI: 10.1007/s11663-007-9101-y

I. INTRODUCTION

THE formation of cavity or raceway in the gas cross-flow condition is common in various industrial processes such as blast furnace, COREX process, granular drying, *etc*. The size and shape of the raceway plays a very important role in the distribution of the gas flow within the bed. Hence, it affects the overall heat and mass transfer within the bed.

Due to the importance of raceway, it has been an area of research interest since the middle of the last century. Many investigators studied the raceway phenomena and proposed a few correlations based on their experimental (cold[1–4] and hot[5,6] model) and theoretical studies.[3,7–10] One of the earliest mathematical models was developed by Szekeley *et al*.[3] based on simple force balance between the gas drag and the bed weight on the raceway roof, ignoring the frictional forces. MacDonald and Bridgewater[7] studied the formation of cavity in the stationary and moving bed under the gas cross-flow condition. Though they reported the importance of frictional force in the cavity formation, they did not consider it in their analysis due to the complexity. Apte *et al*.[8] studied the one-dimensional (1-D) stress distribution above the cavity formed by a vertical air jet introduced at the bottom of the bed. They had considered the force balance between the frictional forces, gas drag, and the bed weight along the tuyere axis. Takahashi *et al*.[9] studied the stress distribution and the buoyancy force at the lower part of blast furnace assuming deadman as a conical body. They calculated vertical normal stress near the raceway boundary at the tuyere level. Rajneesh *et al*.[10] explained cavity formation considering the elemental force balance between the frictional forces, gravity force, and the gas pressure gradient, which is nothing but the manifestation of the gas drag force under gas cross-flow condition. They divided the entire system into two regions, Cartesian and Radial region. In their 1-D analysis they considered the frictional forces of two sidewalls, which were acting over the cross-sectional area. They pointed out that for better prediction of raceway size and shape a two-dimensional (2-D) model is essential.

Solution of 2-D stress field in presence of gas flow has been a challenge since 1976.[11] Plasticity theory (Mohr–Coulomb failure criteria) is widely used to calculate the stresses for designing the storage vessels for granular material (packed bed) both in 1-D and 2-D cases.[12] A 2-D stress analysis in the presence of fluid flow in a moving bed has been carried out by Grossman,[11] where the wall stress was calculated for 1-D case under the uniform axial flow condition. Pressure drop was considered between the two end points and the pressure term in the governing equation was omitted.

In this study, an attempt has been made to predict the stress distribution at the raceway boundary under the gas cross-flow condition from 2-D stress and gas flow analysis. Stresses are found in the presence of fluid flow from a complete 2-D analysis. Plasticity theory is used to get the stress along the slip planes. Pressure profiles are obtained by solving Navier–Stokes equations coupled with k-ε turbulence model. The effective stress is calculated by subtracting the pore pressure from the total stress. Results have been validated against the experiments. It is observed that the raceway boundary is an isostress boundary.

S. SARKAR, formerly Graduate Student, Department of Materials Engineering, Indian Institute of Science, is Postdoctoral Fellow, Fundamentals of Chemical Reaction Engineering, Faculty of Science and Technology, University of Twente, 7522 LD, Enschede, The Netherlands. G.S. GUPTA, Associate Professor, is with the Department of Materials Engineering, Indian Institute of Science, Bangalore 560 012, India. Contact e-mail: govind@materials.iisc.ernet.in
Manuscript submitted October 25, 2006.
Article published online November 29, 2007.

II. THEORETICAL ANALYSIS

A 2-D mathematical model in the Cartesian coordinate system has been developed to study the raceway size and shape based on the following assumptions.

(1) Gas and solid phases exist as interpenetrating continuum.
(2) Gas flow is incompressible and steady state.
(3) Solid granular material is ideal Coulomb material.
(4) Movement of solid particle within the raceway is negligible.

With these assumptions, the stress model has been developed and the governing equations are as follows.

A. *Particle Phase*

Figure 1 shows various forces or stresses acting on a small element PQRS of a 2-D bed. The normal stresses, σ_{xx}, act on planes PS and QR and the shear stresses, τ_{xy}, act on the same planes, but in a direction parallel to the y-axis. Similarly, the direction of σ_{yy} and τ_{yx} are defined. Other forces acting on the element are the fluid drag manifested by a pressure gradient and the gravitational force. Gravitational force is acting in the downward direction at the center of the control volume shown in Figure 1. Therefore, the governing equations for particle phase[11–13] become

$$\frac{\partial \sigma_{xx}}{\partial x} + \frac{\partial \tau_{yx}}{\partial y} + \varepsilon_g \frac{\partial P}{\partial x} = 0 \qquad [1]$$

$$\frac{\partial \sigma_{yy}}{\partial y} + \frac{\partial \tau_{xy}}{\partial x} + \varepsilon_g \frac{\partial P}{\partial y} = \rho_b g \qquad [2]$$

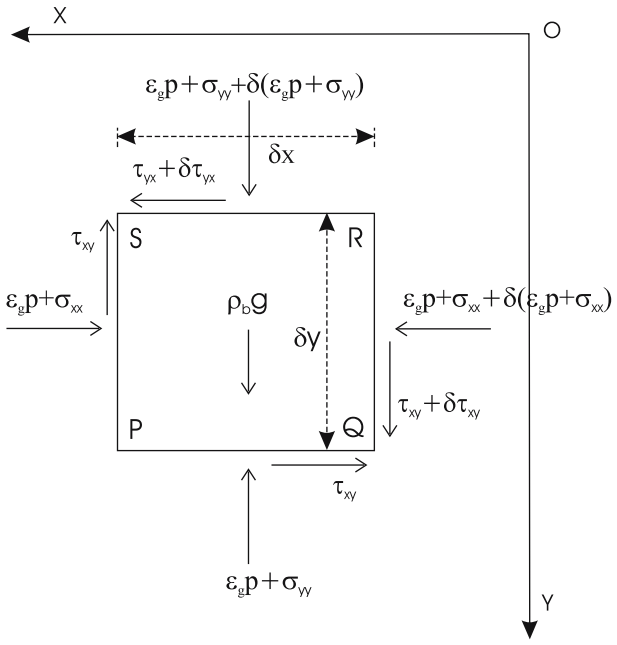

Fig. 1—Schematic representation of stresses on an element.

At equilibrium $\tau_{xy} = \tau_{yx}$. The third term in the above equations shows the effect of pore pressure in the solid force balance equation where P is the gas pressure, ε_g is the bed porosity, ρ_b is the bulk density, and g is the acceleration due to the gravity. To get the pore pressure, momentum equations are solved under turbulent conditions and the governing equations for the gas phase[14,15] are given by the following.

B. *Gas Phase*

Conservation of mass:

$$\frac{\partial(\varepsilon_g u)}{\partial x} + \frac{\partial(\varepsilon_g v)}{\partial y} = 0 \qquad [3]$$

Conservation of momentum along x-direction (u):

$$\begin{aligned}&\frac{\partial(\varepsilon_g \rho_g uu)}{\partial x} + \frac{\partial(\varepsilon_g \rho_g uv)}{\partial y} \\ &= \frac{\partial}{\partial x}\left(\varepsilon_g \mu_e \frac{\partial u}{\partial x}\right) + \frac{\partial}{\partial y}\left(\varepsilon_g \mu_e \frac{\partial u}{\partial y}\right) - \varepsilon_g \frac{\partial p}{\partial x} - \frac{2}{3}\rho_g \varepsilon_g \frac{\partial k}{\partial x} \\ &\quad + \frac{\partial}{\partial x}\left(\varepsilon_g \mu_e \frac{\partial u}{\partial x}\right) + \frac{\partial}{\partial y}\left(\varepsilon_g \mu_e \frac{\partial v}{\partial x}\right) - F_x \end{aligned} \qquad [4]$$

Conservation of momentum along y-direction (v):

$$\begin{aligned}&\frac{\partial\left(\varepsilon_g \rho_g uv\right)}{\partial x} + \frac{\partial\left(\varepsilon_g \rho_g vv\right)}{\partial y} \\ &= \frac{\partial}{\partial x}\left(\varepsilon_g \mu_e \frac{\partial v}{\partial x}\right) + \frac{\partial}{\partial y}\left(\varepsilon_g \mu_e \frac{\partial v}{\partial y}\right) - \varepsilon_g \frac{\partial p}{\partial y} - \frac{2}{3}\rho_g \varepsilon_g \frac{\partial k}{\partial y} \\ &\quad + \frac{\partial}{\partial y}\left(\varepsilon_g \mu_e \frac{\partial v}{\partial y}\right) + \frac{\partial}{\partial x}\left(\varepsilon_g \mu_e \frac{\partial u}{\partial y}\right) - F_y \end{aligned} \qquad [5]$$

Turbulent kinetic energy (k):

$$\begin{aligned}\frac{\partial(\varepsilon_g \rho_g uk)}{\partial x} + \frac{\partial(\varepsilon_g \rho_g vk)}{\partial y} &= \frac{\partial}{\partial x}\left(\varepsilon_g \frac{\mu_t}{\sigma_k}\frac{\partial k}{\partial x}\right) + \frac{\partial}{\partial y}\left(\varepsilon_g \frac{\mu_t}{\sigma_k}\frac{\partial k}{\partial y}\right) \\ &\quad + \varepsilon_g G - \rho_g \varepsilon_g \varepsilon \end{aligned} \qquad [6]$$

Rate of dissipation of turbulent kinetic energy (ε):

$$\begin{aligned}\frac{\partial(\varepsilon_g \rho_g u\varepsilon)}{\partial x} + \frac{\partial(\varepsilon_g \rho_g v\varepsilon)}{\partial y} &= \frac{\partial}{\partial x}\left(\varepsilon_g \frac{\mu_t}{\sigma_z}\frac{\partial \varepsilon}{\partial x}\right) + \frac{\partial}{\partial y}\left(\varepsilon_g \frac{\mu_t}{\sigma_z}\frac{\partial \varepsilon}{\partial y}\right) \\ &\quad + \frac{\varepsilon}{k}\left(c_1 \varepsilon_g G - c_2 \rho_g \varepsilon_g \varepsilon\right) \end{aligned} \qquad [7]$$

Fluid and particle interaction force along x-direction in Eq. [4] is given by

$$F_x = (a|V| + b|V|u) \qquad [8]$$

Fluid and particle interaction force along y-direction in Eq. [5] is expressed as

$$F_y = (a|V| + b|V|v) \qquad [9]$$

where velocity magnitude is given by

$$|V| = \sqrt{u^2 + v^2} \qquad [10]$$

Turbulent (μ_t) and effective (μ_e) viscosities are given by

$$\mu_t = \frac{c_\mu \rho_g k^2}{\varepsilon} \quad \text{and} \quad \mu_e = \mu_g + \mu_t \qquad [11]$$

and

$$G = \mu_t \left\{ 2\left[\left(\frac{\partial u}{\partial x}\right)^2 + \left(\frac{\partial v}{\partial y}\right)^2 \right] + \left[\left(\frac{\partial u}{\partial y}\right) + \left(\frac{\partial v}{\partial x}\right) \right]^2 \right\} \qquad [12]$$

The values of constants used in the turbulent model are

$$c_\mu = 0.09,\ \ c_1 = 1.44,\ \ c_2 = 1.92,\ \ \sigma_k = 1.0,\ \text{and}\ \sigma_\varepsilon = 1.3 \qquad [13]$$

where u and v are the velocities in x and y directions, respectively; ρ is the density; and μ_g is the viscosity of gas. Also, k is the turbulent kinetic energy, ε is the dissipation rate of turbulent kinetic energy, and μ_e is the effective viscosity of the turbulent flow. Momentum transfer due to the gas-solid interaction along the x and y directions (Eqs. [4] and [5]) has been modeled as F_x and F_y, respectively. In Eqs. [8] and [9], a and b are constants and have been evaluated based on either Ergun's equation when $\varepsilon_g \le 0.8$ (Eq. [14]) or Richardson and Zaki's formulation (Eq. [15]).

$$a = 150\frac{(1-\varepsilon_g)^2 \mu_g}{\varepsilon_g d_p^2}; \quad b = 1.75\frac{(1-\varepsilon_g)\rho_g}{\varepsilon_g^3 d_p} \quad \varepsilon_g \le 0.8 \qquad [14]$$

$$a = 0;\ b = \frac{3}{4} C_d \frac{(1-\varepsilon_g)\varepsilon_g^{-1.65}\rho_g}{d_p} \quad \varepsilon_g > 0.8 \qquad [15]$$

where the drag coefficient, C_d, is related to the particle Reynolds number, Re_p, by the following equations:[15]

$$C_d = \frac{24}{\mathrm{Re}_p}\left[1 + 0.15(\mathrm{Re}_p)^{0.687}\right] \quad \mathrm{Re}_p \le 1000 \qquad [16]$$

$$C_d = 0.44 \quad \mathrm{Re}_p > 1000 \qquad [17]$$

$$\mathrm{Re}_p = \frac{\varepsilon_g \rho_g |V| d_p}{\mu_g} \qquad [18]$$

Now the concept of total stress and effective stress will be introduced and are given by the following equation:[13]

$$\begin{aligned} \sigma'_{xx} &= \sigma_{xx} + \varepsilon_g P \\ \sigma'_{yy} &= \sigma_{yy} + \varepsilon_g P \end{aligned} \qquad [19]$$

where σ'_{xx} and σ'_{yy} are the total normal stresses along the x and y directions, respectively, and σ_{xx} and σ_{yy} are the respective effective normal stresses along the x and y directions. The pore pressure is represented by $\varepsilon_g P$. The state of effective and total stress has been represented using Mohr circle in Figure 2. It also shows internal yield locus (IYL) or coulomb line. When IYL touches the Mohr circle, the material is said to be in a state of incipient slip or incipient failure.

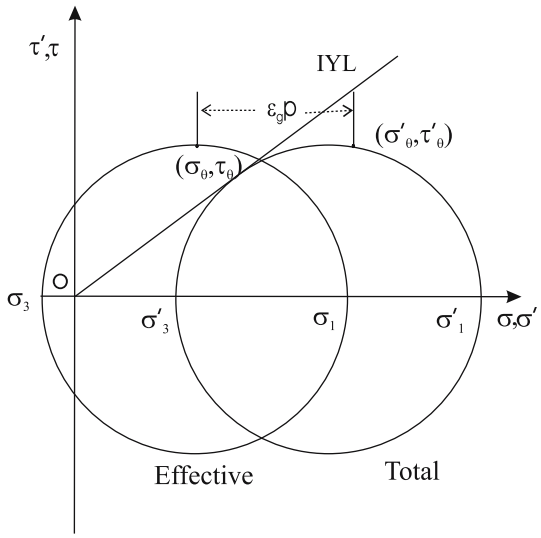

Fig. 2—Mohr circles for effective and total stresses.

Due to the development of pore pressure, $\varepsilon_g P$, Mohr circle for the total stresses has been shifted toward the left and has been marked as Mohr circle for the effective stresses. If the total normal and shear stresses on a plane are given by σ'_θ and τ'_θ, respectively, then the effective normal and shear stresses would be σ_θ and τ_θ, respectively, due to the development of pore pressure. In Figure 2, a point has been marked on the total stress Mohr circle $(\sigma'_\theta, \tau'_\theta)$. That point has been shifted toward the left and has been marked as $(\sigma_\theta, \tau_\theta)$ on the effective stress Mohr circle due to development of the pore pressure. The major and minor principal effective stresses are σ_1 and σ_3, and σ'_1 and σ'_3 are the major and minor principal total stresses, respectively. It can be seen that due to the development of pore pressure, the normal stress has reduced but the shear stress is same (*i.e.*, $\tau'_{xy} = \tau_{xy}$). The total shear stress is τ'_{xy}.

In order to solve Eqs. [1] and [2], one additional equation is required. Assuming that the material is in a state of incipient or actual yield, Mohr–Coulomb yield criterion has been used here. It has also been assumed that the total stress obeys Mohr–Coulomb criterion which is given subsequently.[11–13]

$$\frac{\left(\sigma'_{yy} - \sigma'_{xx}\right)^2 + 4\tau'^2_{xy}}{\left(\sigma'_{yy} + \sigma'_{xx}\right)^2} = \frac{\mu^2}{1+\mu^2} \qquad [20]$$

where σ'_{xx}, σ'_{yy}, and τ'_{xy} can be written in terms of two variables as

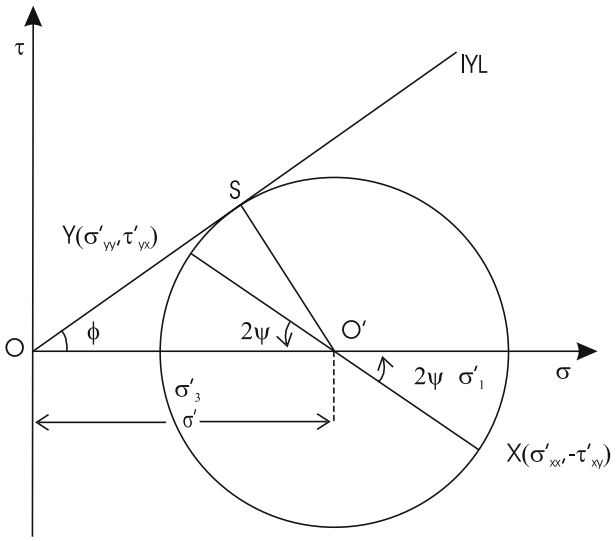

Fig. 3—Definition of stress parameters.

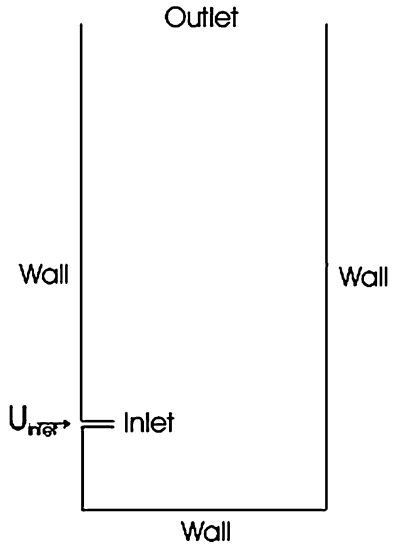

Fig. 4—Computational domain boundary.

$$\sigma'_{xx} = \sigma'(1 + \sin\phi\cos 2\psi)$$
$$\sigma'_{yy} = \sigma'(1 - \sin\phi\cos 2\psi) \quad [21]$$
$$\tau'_{xy} = \sigma' \sin\phi \sin 2\psi$$

where ϕ is the static angle of friction, ψ is the angle measured anticlockwise from the x plane to the major principal stress direction, and μ is the coefficient of friction. All of these parameters are shown in Figure 3.

Equation [21] automatically satisfies the limiting equilibrium condition or yield criteria (Eq. [20]), and σ' is the distance from the center of the Mohr circle to the point where Coulomb line meets the σ-axis and is given as

$$\sigma' = \frac{\sigma'_{xx} + \sigma'_{yy}}{2} \quad [22]$$

Now σ'_{xx} and σ'_{yy} (total stress) are nothing but stress distribution when pressure is zero (*i.e.*, stress distribution before the fluid starts entering into the system), and it obeys Mohr–Coulomb's law. Thus, essentially the stress distribution in the absence of fluid flow can be solved and the effective stress can be obtained by subtracting the pore pressure from the total stress as it is given in Eq. [19].

III. BOUNDARY CONDITIONS

Figure 4 shows the computational domain boundary. The gas phase boundary conditions are specified as follows. At the inlet, all the dependable variables are known and are given as $u = u_{\text{inlet}}$, $v = 0$, $k = 0.005u^2_{\text{inlet}}$, and $\varepsilon = (0.005u^2_{\text{inlet}})^{1.5}/\text{l}_\text{m}$. At the outlet, pressure has been set to atmospheric pressure, $u = 0$, and zero normal gradient for k and ε.

For wall boundary (except inlet and outlet), $v = 0$, $u = 0$, zero normal gradient for k and ε, and $lm = (0.33w)/2$, where l_m is the mixing length and w is the opening of the tuyere slot.

Boundary conditions for particle phase are given as follows: At the top (outlet), all the stress components are zero and at the sidewall $\tau_{xy} = \mu\sigma_x$. In terms of σ and Ψ, at the top, $\sigma = 0.0$ and $\Psi = 1.57$ radian (assuming active failure), and at the wall, $\Psi = \Psi_w = 180 + \varpi - \phi w$ or $= 180 - \varpi + \phi_w$, where $\varpi = \sin^{-1}(\sin\phi_w/\sin\phi)$.

Once the total stress distribution $(\sigma'_{xx}, \sigma'_{yy}, \tau'_{xy})$ is known, the stress distribution along the slip plane can be found as the slip plane lies at $\Psi \pm \varepsilon_c$, where distribution of Ψ is also known and ε_c is given by $\varepsilon_c = (90-\phi)/2$. The following equations were used to get the total stress (normal and shear) distribution at the slip plane.

$$\sigma' = \frac{1}{2}\left(\sigma'_{xx} + \sigma'_{yy}\right) + \frac{1}{2}\left(\sigma'_{xx} - \sigma'_{yy}\right)\cos 2\Psi - \tau'_{xy}\sin 2\Psi \quad [23]$$

$$\tau' = \frac{1}{2}\left(\sigma'_{xx} - \sigma'_{yy}\right)\sin 2\Psi - \tau'_{xy}\cos 2\Psi \quad [24]$$

IV. COMPUTATIONAL TECHNIQUE

The partial differential equations for the gas phase are discretized using staggered grid control volume technique.[16,17] The power-law scheme has been used to evaluate the convective transport term in the above equations. Discretized equations were solved using semi-implicit method for pressure-linked equations (SIMPLE) algorithm with suitable boundary conditions. Tri-diagonal matrix algorithm (TDMA) has been used as a solver to get the solutions. Global mass balance was put as a convergence criteria *i.e.*, ((mass in – mass out)/mass in) < 0.001. Near the tuyere, grid size was

5×5 mm and away from the tuyere, grid size was 6×6 mm. These grid sizes were chosen after ensuring that the solution is independent of grid size.

Particle phase equations were solved using the method of characteristics.[12,18] In this method, partial differential equations are reduced to ordinary differential equations along some particular paths, which are called characteristics. Those lines are generally called α and β characteristics. The equation of α characteristic is expressed by

$$\frac{dy}{dx} = \tan\ (\Psi - \varepsilon_c) \qquad [25]$$

Similarly, the equation for β characteristic is given by

$$\frac{dy}{dx} = \tan\ (\Psi + \varepsilon_c) \qquad [26]$$

The normal stresses presented here are on the characteristic lines or slip planes unless it is mentioned otherwise. Computer code was developed in Fortran-90. Simulation parameters are given in Section VI wherever they are required.

V. EXPERIMENT

In order to validate the predictions of the mathematical model, experiments were carried out in a 2-D model. A schematic diagram of the experimental setup is shown in Figure 5. It was made of 10-mm-thick Perspex sheet. The model was 1800-mm high, 600-mm wide, and 60-mm thick. It was supported by iron bar reinforcement to prevent outward bulging. The tuyere opening was 5 mm, which protruded 50 mm inside the bed across the entire thickness of the bed, *i.e.*, it was a slot tuyere. There was a stainless steel screen support at the bottom of the packed bed. Spherical plastic beads of 5.8-mm diameter were used during the experiments as it gave reasonable sized raceways before fluidization occurs above the raceway.

The bed was filled with plastic beads up to 1 m height from the tuyere level. Room-temperature compressed air was used as a gas, which was blown into the rig. The flow rate was measured using a variable area flow meter corrected for any pressure effects. The inlet velocity of air at the tuyere varied from 0 to 103 m/s. In order to measure the pressure at various points within the bed, 6-mm-diameter pressure-taping holes, each 10 cm apart, were made along the bed height. The holes were 6 cm away from the tuyere sidewall. Near the raceway, these holes were 3 cm apart. At the tuyere level, along the width and around it some holes were made to get the pressure distribution. These holes were connected to pressure transducers and manometers. Pressure transducers were connected to a computer through data logger. All of the experimental data reported here are an average of at least three experiments.

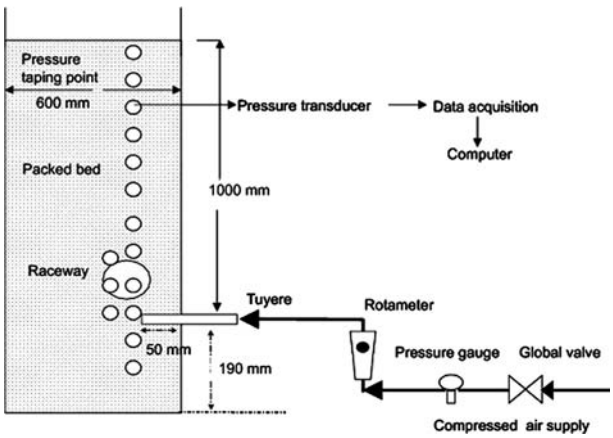

Fig. 5—Schematic diagram of the experimental setup.

VI. RESULTS AND DISCUSSION

Figure 6 shows the velocity vector plots at inlet gas velocity of 103 m/s. Tuyere protrusion is also shown in the figure. Simulation parameters are given in Table I. It is observed from the figure that the gas enters through the tuyere at high velocity, spreads quickly inside the bed with a uniform velocity, and escapes from the top of

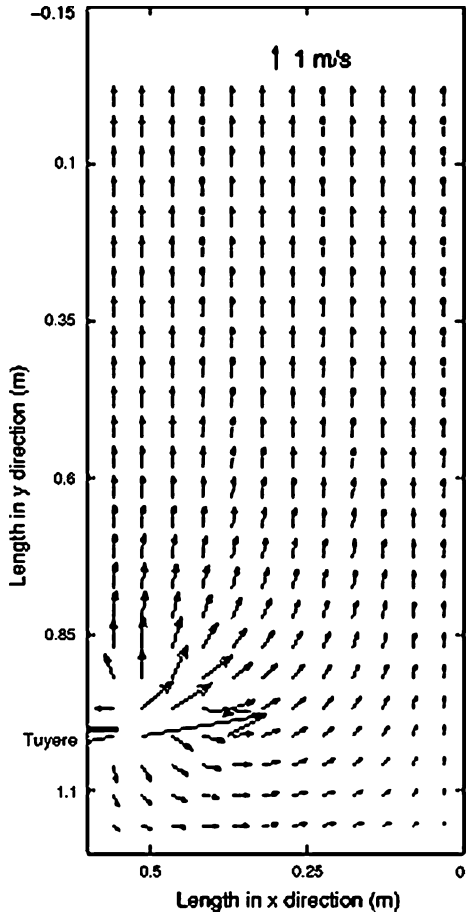

Fig. 6—Computed velocity distribution at 103 m/s inlet blast velocity, bed height = 1.2 m, bed width = 0.6 m, diameter of plastic beads = 5.8 mm, and tuyere opening = 5 mm.

the bed. The gas velocity becomes almost constant (about 0.85 m/s) at an approximate distance of 0.2 m from the tuyere level. It seems the gas is spreading out radially, with the tuyere exit being the center. This finding supports 1-D analysis of other researchers,[10] in which it is assumed that gas velocity becomes constant after a certain distance from the tuyere level. However, it seems 1-D analysis would slightly underestimate this distance compared to the 2-D analysis.

Figure 7 shows an enlarged portion of Figure 6, which includes tuyere zone. Velocity at the tuyere exit is 103 m/s, as indicated by the largest arrow. In front of the tuyere, it reduces to about 60 m/s. Near the tuyere, gas spreads radially, and about 2 cm from the tuyere tip, it reduces to 2 m/s or lower.

Figure 8 shows the experimental pressure distribution at different inlet gas velocities along the bed height at 0.06 m away from the tuyere sidewall. Tuyere is located at 0.2 m above the bottom of the bed as marked by the arrow in Figure 8 and it is protruded 0.05 m inside the bed. Theoretical results obtained by the model under similar operating conditions are also shown in this figure. A good agreement between the two lends support to the gas flow model developed in this study. It can also be seen that maximum pressure is in front of the tuyere and it decreases as one goes either side of it (*i.e.*, above

Table I. Parameters Used in Other Simulations

Parameters	Value
Bed length	1.2 m
Bed width	0.6 m
Void fraction within the bed (ε_g)	0.47
Internal angle of friction	30.65 deg
Wall angle of friction	10.76 deg
Particle diameter	0.0058 m
Density of gas	1.178 kg/m^3
Viscosity of gas	1.983e^{-5} Pa·s
Density of the particle	1080 kg/m^3
Void fraction within the raceway (ε_r)	$\varepsilon_r = 1.0$ for $\sigma < 0.0$ $\varepsilon_r = 1.0 + ((0.5–1.0)/(\sigma_r - 0.0))*\sigma$ for ($\sigma > 0.0$ and $\sigma < \sigma_r$)

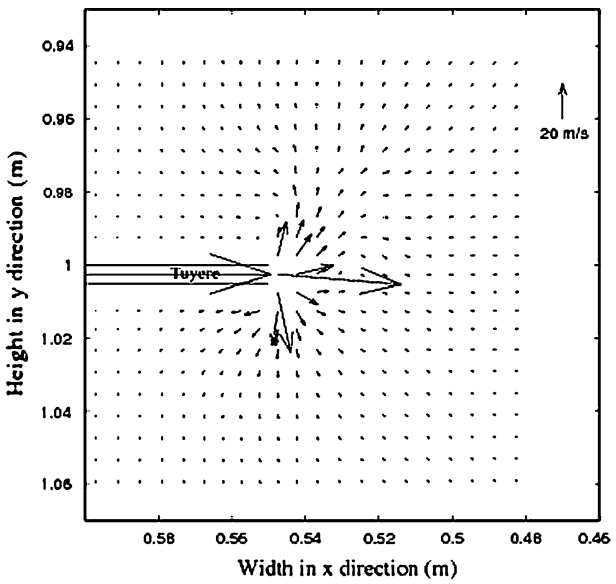

Fig. 7—Computed velocity distribution at 103 m/s inlet blast velocity near the tuyere, bed height = 1.2 m, bed width = 0.6 m, diameter of plastic beads = 5.8 mm, and tuyere opening = 5 mm.

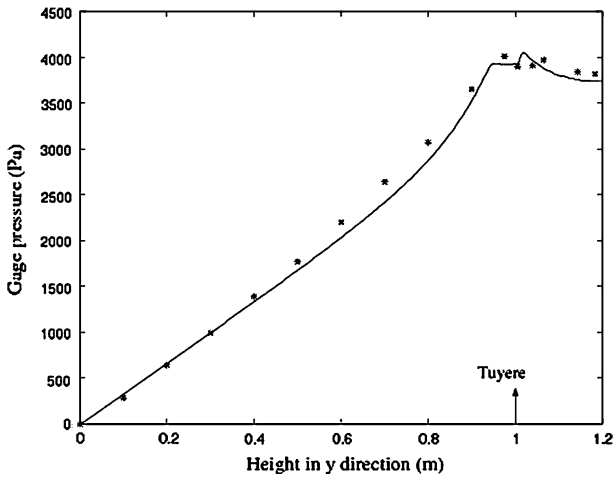

Fig. 8—Comparison of theoretical and experimental pressure profile at 103 m/s inlet blast velocity, bed height = 1.2 m, bed width = 0.6 m, diameter of plastic beads = 5.8 mm, and tuyere opening = 5 mm.

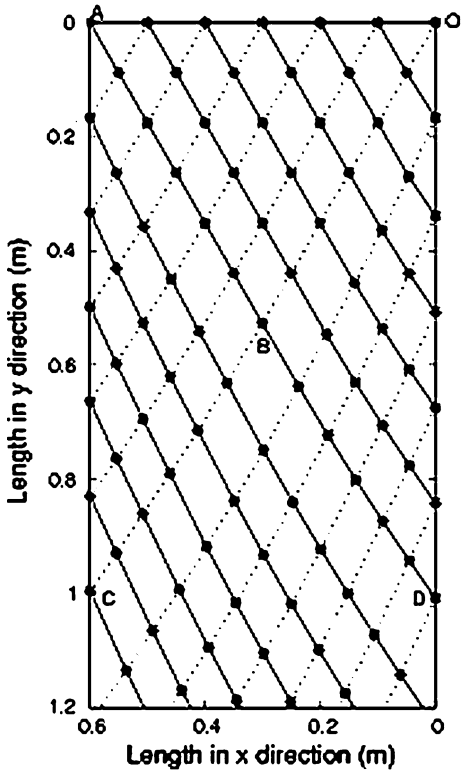

Fig. 9—Computed α-(dotted lines) and β-(solid lines) slip planes, bed height = 1.2 m, bed width = 0.6 m, and diameter of plastic beads = 5.8 mm.

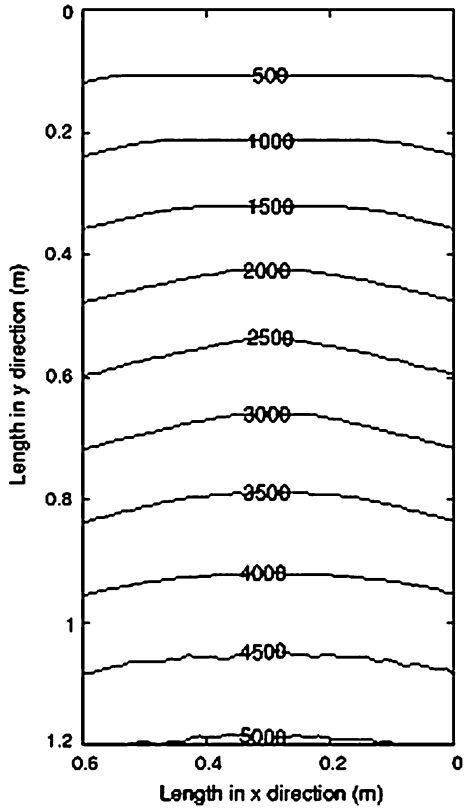

Fig. 10—Computed total normal stress on α-slip plane, bed height = 1.2 m, bed width = 0.6 m, and diameter of plastic beads = 5.8 mm.

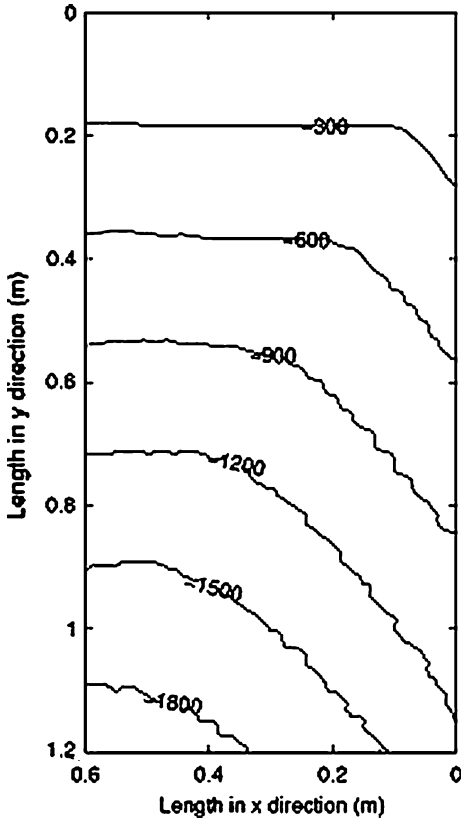

Fig. 11—Computed shear stress on α-slip plane, bed height = 1.2 m, bed width = 0.6 m, and diameter of plastic beads = 5.8 mm.

or below the tuyere). Below the tuyere, pressure gradient is less than that above it, as bottom of the apparatus is closed.

The results of stress analysis are shown in Figures 9–14. Figure 9 shows the possible slip planes. Parameters, which have been used in simulation, are given in Table I. Dotted lines and solid lines represent α- and β-slip planes, respectively, and the star represents the point where two characteristics meet each other. The region bounded by OAB in the figure shows the zone where stress is being transferred from the top only. The effect from both sidewalls is not felt. The effect of stress from the top as well as from the left and right sidewall is felt in the regions bounded by ABC and OBD, respectively. Below BCD the effect from both sidewalls is present (effect of stress from the top is not directly transferred). One can observe that at the points where characteristic lines cut the wall, a new family of characteristics generate and transmit the information of that point.

Figures 10 and 11 show the total normal and shear stress distribution along α-slip plane, respectively. The total normal and shear stress distribution along β plane are given in Figures 12 and 13, respectively. From these figures it can be seen that along both slip planes normal stresses are positive and the same in the magnitude. However, the shear stresses are different and opposite in direction. This can be explained using Figure 14, where it can be seen that there are two incipient slip planes (S and S′) at the critical stability, which have the same normal stress. However, though the magnitudes are same, the shear stresses are opposite in direction. The magnitude of shear stress in the figure increases from top to bottom of the bed and also toward the left sidewall for α-slip plane. For β-slip plane the magnitude of shear stress increases toward the right sidewall from the top to the bottom. The magnitude of the normal stress is the maximum at the center of the bed in both the cases and increases from top to bottom.

The results on normal stress, which are reported in this section, are on the slip plane to avoid any confusion about the active or passive failure. Therefore, total normal stress on the slip plane will be used as normal stress or stress throughout in this article.

In order to validate the stress model, theoretical vertical stress profile under the static condition at the bottom has been compared with published experimental stress profile and is shown in Figure 15. All the parameters used in the simulation are taken from Reference 19 and are mentioned in Table II. There is an excellent match between the theoretical and experimental vertical stress profile, which validates the current stress model.

The vertical stress profiles in the bed, under similar conditions as in Figure 15, are shown in Figure 16. Note that the vertical normal stress is more at the center when going from top to bottom. Unfortunately, experimental data are not available in the literature for comparison.

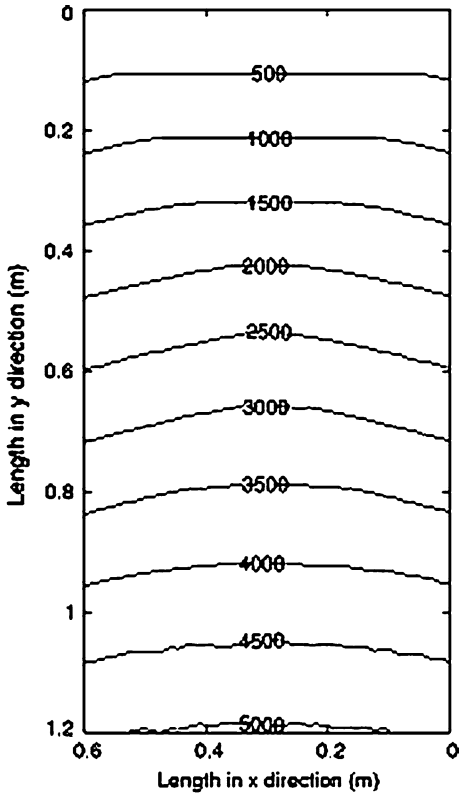

Fig. 12—Computed total normal stress on β-slip plane, bed height = 1.2 m, bed width = 0.6 m, and diameter of plastic beads = 5.8 mm.

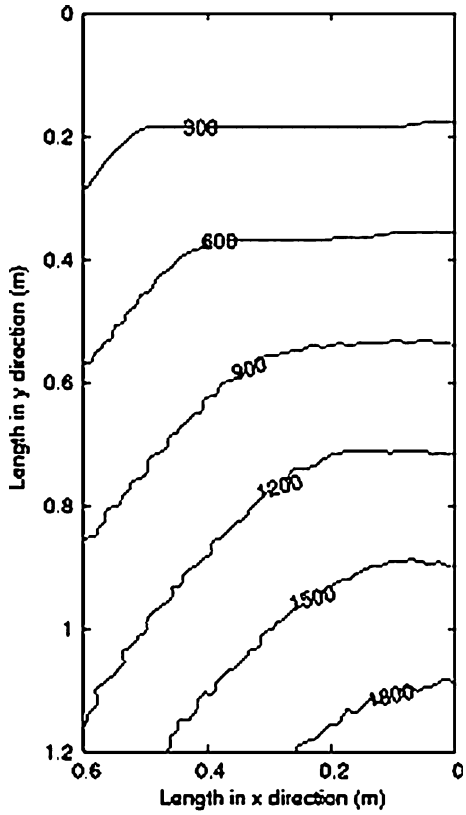

Fig. 13—Computed shear stress on β-slip plane, bed height = 1.2 m, bed width = 0.6 m, and diameter of plastic beads = 5.8 mm.

After validating both the gas flow and stress models, either with experiments or against published data, full analysis of the stress and pressure was conducted for the actual experimental conditions as described in Section V. Stresses were computed in the presence of gas flow. In all of the simulations, a relation between the void fraction and normal stress in the raceway region was used, which is given in Table I. This relationship was obtained based on the analysis of void fraction results given by various researchers.[20]

Figure 17 shows the normal stress distribution at 103 m/s inlet gas velocity on slip planes. Near the tuyere region stress goes below zero, which implies the absence of particles in this region. Moving away from the tuyere region (above the tuyere axis/level) the normal stresses start increasing to a certain distance and then start decreasing. However, the magnitude of stresses above and below the tuyere level is always lower than the magnitude of stresses computed in the absence of gas flow (Figures 10 and 12 under similar conditions). The reason is that in the presence of gas flow the weight of the burden is not transferred as much as it was transferred before (without the gas flow). That is to say that gas drag is playing an important part in the stress analysis and cannot be ignored.

Pressure distribution at 103 m/s inlet blast velocity is given in Figure 18. Maximum pressure is found at the tip of the tuyere and decreased moving away from the tuyere. It decreases more rapidly above the tuyere than along the tuyere axis or below it. Pressure drop becomes almost constant above 20 cm from the tuyere level.

Figure 19 shows the normal stress distribution (along the slip plane) at the raceway boundary at 103 m/s in increasing inlet gas blast velocity condition. In this simulation experimental raceway size and shape was used as an input parameter. Stars with dotted line show the experimental raceway and the solid line is the stress contour. It is found that stress contour of 1500 Pa is exactly lying over the experimental raceway boundary. Due to the movement of the particles near the raceway boundary, the stress along the raceway boundary fluctuates fast in the range of ± 200 Pa. It is obvious from this figure that raceway boundary is an isostress boundary, which is an important finding and may be used to evaluate the raceway shape and size in other packed bed processes.

It should be noted that in 3-D studies, Mohr–Coulomb criterion becomes invalid. Therefore, the proposed stress model could be used in the 3-D case, considering axisymmetry in one of the directions. Also, the discrete element method (DEM) approach[21] can be used to solve the problem. However, due to limitations of existing computational power, it is not possible to use DEM to simulate the real blast furnace in the near future.

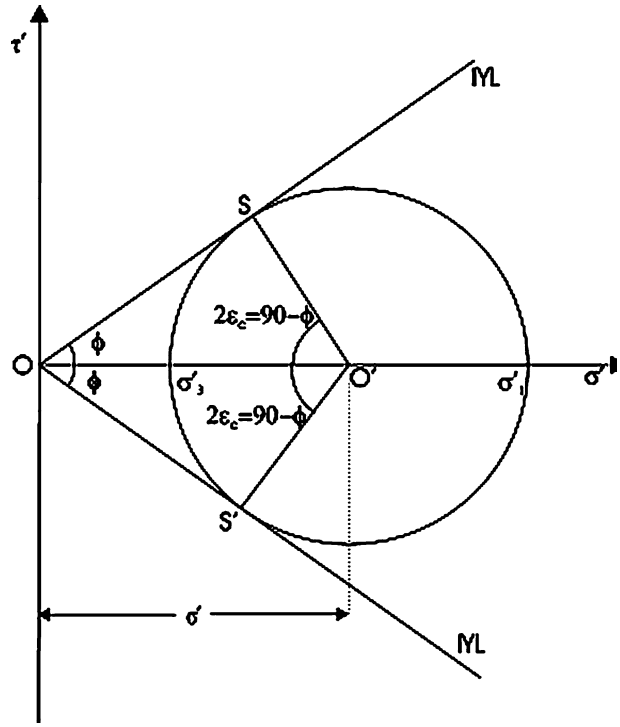

Fig. 14—Mohr–Coulomb failure criterion.

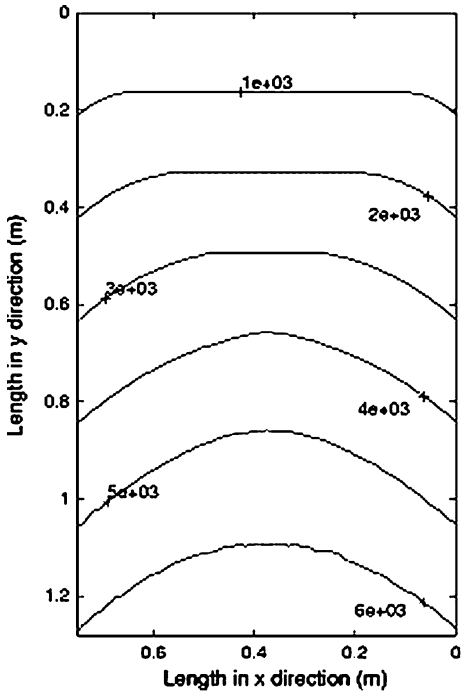

Fig. 16—Computed vertical stress distribution (Katayama *et al.*[19]) throughout the bed, bed height = 1.285 m, and bed width = 0.75 m.

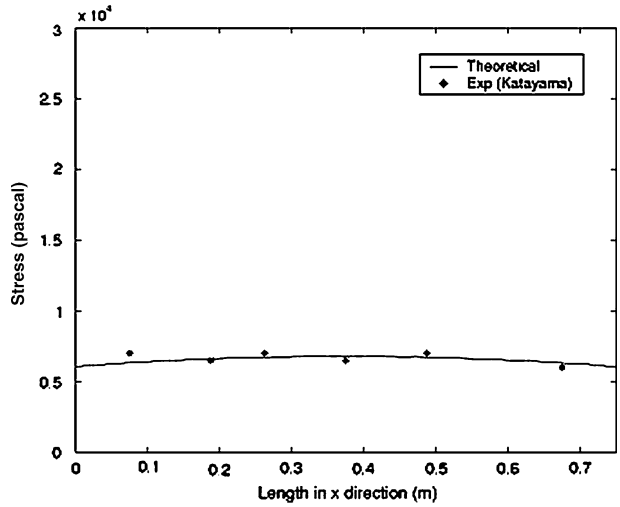

Fig. 15—Comparison of theoretical and experimental[19] vertical stress profile, bed height = 1.285 m, and bed width = 0.75 m.

Table II. Parameters Used in the Simulations for Validation of Stress Profile[19]

Parameters	Value
Bed length	1.285 m
Bed width	0.75 m
Internal angle of friction	32 deg
Wall angle of friction	20 deg
Bulk density	620 kg/m^3

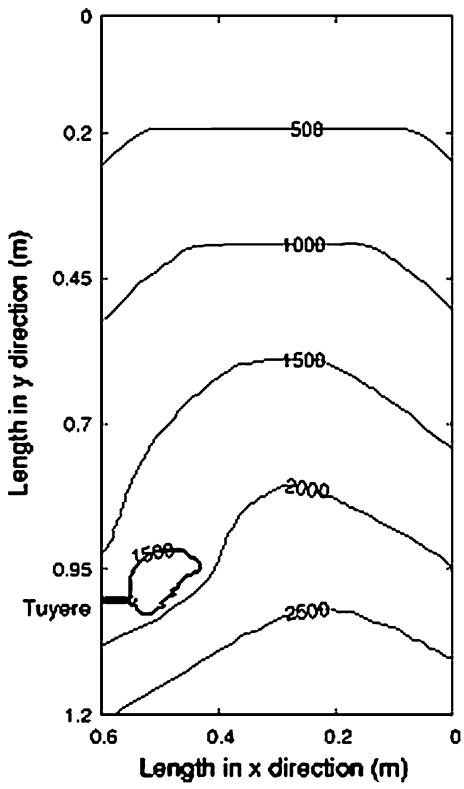

Fig. 17—Computed stress distribution at 103 m/s inlet blast velocity, bed height = 1.2 m, bed width = 0.6 m, diameter of plastic beads = 5.8 mm, and tuyere opening = 5 mm.

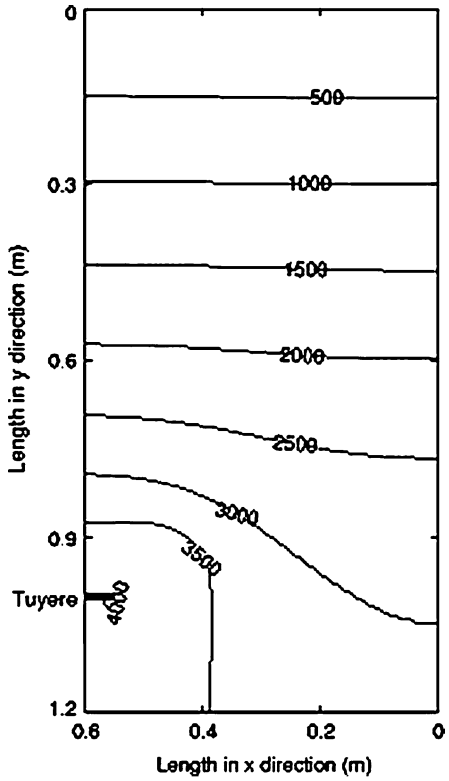

Fig. 18—Computed pressure distribution at 103 m/s inlet blast velocity, bed height = 1.2 m, bed width = 0.6 m, diameter of plastic beads = 5.8 mm, and tuyere opening = 5 mm.

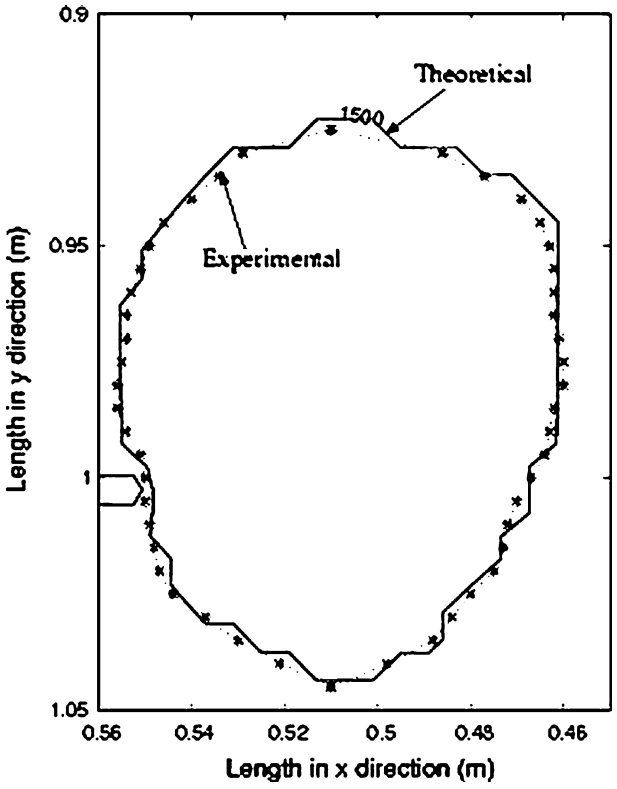

Fig. 19—Isostress contours of raceway (computed and experimental) at 103 m/s inlet blast velocity, bed height = 1.2 m, bed width = 0.6 m, diameter of plastic beads = 5.8 mm, and tuyere opening = 5 mm.

VII. CONCLUSIONS

A 2-D mathematical model has been developed to predict the stress distribution along the raceway boundary. Stresses are presented along the slip planes and it is found that normal stress along both the slip planes are the same but shear stresses are different and opposite in direction. The theoretical stress profile matches very well with published experimental vertical stress profile and agreement between the computed and experimental pressure profile is good, which lends support to the model. Computed results show that gas drag substantially contributes in supporting the packed bed and thus reducing the stress in the entire bed. It is also found that the raceway boundary is an isostress boundary.

NOMENCLATURE

x	length in horizontal direction (m)
y	length in vertical direction (m)
u_x	gas velocity along x direction (m/s)
u_y	gas velocity along y direction (m/s)
k	turbulent kinetic energy of the blast (m^2/s^2)
g	acceleration due to gravity (m/s^2)
P	gas pressure (Pa)
l_m	mixing length (m)
w	tuyere opening (m)
Re_p	particle Reynolds number (dimensionless)
c_d	drag coefficient
d_p	particle diameter (m)
c_μ	constant used in the turbulence model (dimensionless)
c_1	constant used in the turbulence model (dimensionless)
c_2	constant used in the turbulence model (dimensionless)
F_x	fluid-particle drag force along x direction (N)
F_y	fluid-particle drag force along y direction (N)

Greek letters

ϕ	internal angle of friction (deg)
ϕ_w	wall angle of friction (deg)
ε	rate of dissipation of turbulent kinetic energy (m^2/s^3)
ρ_g	density of blast gas (kg/m^3)
ρ_b	bulk density (kg/m^3)
μ_g	viscosity of the blast gas (kg/m/s)
ε_g	bed porosity (dimensionless)
ε_r	bed porosity in and around the raceway (dimensionless)
σ_{xx}	normal stress along x direction (Pa)
σ_{yy}	normal stress along y direction (Pa)
σ_r	normal stress on slip plane at raceway boundary (Pa)
τ_{xy}	shear stress along x plane (Pa)
μ	coefficient of friction (dimensionless)
σ'_{xx}	total normal stress along x direction (Pa)

σ'_{yy} total normal stress along y direction (Pa)
τ'_{xy} total shear stress along x plane (Pa)
σ_k constant used in the turbulence model (dimensionless)
σ_ε constant used in the turbulence model (dimensionless)
μ_e effective viscosity of the blast gas (kg/m/s)
μ_t turbulent viscosity (kg/m/s)
σ average of σ'_{xx} and σ'_{yy} (Pa)
σ'_θ total normal stress on any arbitrary plane (Pa)
τ'_θ total normal stress on any arbitrary plane (Pa)
ψ angle measured from x plane to the major principle direction (rad)
ω $\sin^{-1}(\sin\phi_w/\sin\phi)$
ε_c $(90 - \phi)/2$ (rad)

REFERENCES

1. J.F. Elliott, R.A. Bachanan, and J.B. Wagstaff: *Trans. AIME*, 1952, vol. 194, pp. 709–17.
2. J.B. Wagstaff and W.H. Holman: *Trans. AIME*, 1957, Mar., pp. 370–76.
3. J. Szekely and J.J. Poveromo: *Metall. Trans. B*, 1975, vol. 6B, pp. 119–30.
4. P.J. Flint and J.M. Burgess: *Metall. Trans. B*, 1992, vol. 23B, pp. 267–83.
5. M. Hatano, B. Hiraoka, M. Fukuda, and T. Masuike: *Iron Steel Inst. Jpn.*, 1977, vol. 17, pp. 102–09.
6. M. Nakamura, T. Sugiyama, T. Uno, Y. Hara, and S. Kondo: *Tetsu-to-Hagané*, 1977, vol. 63 (1), pp. 28–36.
7. J.F. MacDonald and J. Bridgwater: *Chem. Eng. Sci.*, 1997, vol. 52 (5), pp. 677–91.
8. V.B. Apte, T.F. Wall, and J.S. Truelove: *AIChEJ*, 1990, vol. 36 (3), pp. 461–68.
9. H. Takahashi, H. Kawai, and Y. Suzuki: *Chem. Eng. Sci.*, 2002, vol. 57, pp. 215–26.
10. S. Rajneesh and G.S. Gupta: *Powder Technol.*, 2003, vol. 134, pp. 72–85.
11. G. Grossman: *AIChEJ*, 1975, vol. 21 (4), pp. 720–30.
12. M. Nedderman: *Statics and Kinematics of Granular Materials*, Cambridge University Press, Cambridge, United Kingdom, 1992.
13. K. Terzaghi: *Theoretical Soil Mechanics*, John Wiley & Sons, Inc, New York, NY, 2001.
14. V.B. Apte, T.F. Wall, and J.S. Truelove: *Chem. Eng. Res. Des.*, 1988, vol. 66, pp. 357–62.
15. B.E. Launder and D.B. Spalding: *Comp. Methods Appl. Mech. Eng*, 1974, vol. 3, pp. 269–89.
16. S.V. Patankar: *Numerical Heat Transfer and Fluid Flow*, Hemisphere Science, Washington, DC, 1980.
17. H.K. Versteeg and W. Malalasekera: *An Introduction to Computational Fluid Dynamics The Finite Volume Method*, Pearson Prentice Hall, England, United Kingdom, 1995.
18. M.B. Abbott: *An Introduction to the Method of Characteristics*, Thames and Hudson, London, 1966.
19. K. Katayama, S. Wakabayashi, T. Inada, K. Takatani, and H. Yamaoka: *Tetsu-to-Hagané*, 1997, vol. 83 (2), pp. 91–96.
20. K. Nozawa, T. Kamijo, and M. Shimizu: *Tetsu-to-Hagané*, 1995, vol. 81 (9), pp. 882–87.
21. P.A. Cundall and O.D.L. Stack: *Geotechnique*, 1979, vol. 29 (1), pp. 47–65.